



Mafic–ultramafic and quartz-rich rock indices deduced from ASTER thermal infrared data using a linear approximation to the Planck function



Chao Ding^a, Xiangnan Liu^{a,*}, Wencan Liu^b, Meiling Liu^a, Yao Li^c

^a School of Information Engineering, China University of Geosciences, Beijing 100083, China

^b Institute of Geological Survey, China University of Geosciences, Beijing 100083, China

^c Institute of Remote Sensing and Digital Earth, Chinese Academy of Sciences, Beijing 100094, China

ARTICLE INFO

Article history:

Received 2 August 2013

Received in revised form 10 January 2014

Accepted 13 January 2014

Available online 24 January 2014

Keywords:

Lithologic mapping

ASTER

Thermal infrared

Planck function

Linear regression analysis

Lithologic indices

ABSTRACT

ASTER thermal infrared (TIR) data are widely used to detect mafic–ultramafic rock and quartz-rich rock, and several rock indices have been proposed based on emissivity features. However, ASTER TIR bands of radiance data correlate highly with each other, which indicates that the independent information derived from different bands may be limited, what's more, ASTER TIR radiance-at-sensor data contain atmospheric effect and temperature information, thus interfering with the availability of these previously proposed indices. In this study, we aim to explain the correlation using a linear approximation of the Planck function and deduce a linear equation that represents the relationship of the radiance between two TIR bands. Theoretical difference indices were deduced based on the linear equation and regression residual characteristics for any two ASTER TIR radiance bands. The study area is located in Qinghai Province, China, and belongs to the Qinghai–Tibet Plateau, where the average elevation is approximately 4200 m. A scatter plot of radiance derived from the ASTER image that overlaps the study area indicates that mafic–ultramafic rock and quartz-rich rock can be distinguished from other surface objects well. Two mafic–ultramafic rock indices ($MI_1 = b_{13} - 0.9147 * b_{10} - 1.4366$ and $MI_2 = b_{13} - 0.8945 * b_{11} - 1.2404$) and two quartz-rich rock indices ($QI_1 = b_{13} - 0.9261 * b_{12} - 1.4623$ and $QI_2 = b_{14} - 0.844 * b_{12} - 1.8971$) were proposed; they satisfactorily map these rock units. The atmospheric effect on the indices is weak in arid or high-elevation region, so it will not interfere with the indices obviously in these regions. One-way variance analysis was performed to discuss the stability of the indices with respect to temperature. The mafic–ultramafic rock indices are found to be independent of temperature, whereas the values of quartz-rich rock indices increase with the rising of temperature. We thus conclude that the quartz-rich rock indices are suitable for the high-elevation region only, while the mafic–ultramafic rock indices may be capable of detecting these rocks in regions with different natural conditions.

© 2014 Elsevier B.V. All rights reserved.

1. Introduction

The logistics of conducting geological survey work are always difficult in regions of high elevation, such as Qinghai–Tibet Plateau of China, because of the harsh natural environments found there. Remote sensing can aid in lithologic mapping at macroscopic scales and guide further geological surveys in such places. The Advanced Spaceborne Thermal Emission and Reflectance Radiometer (ASTER) is one of the most widely used remote sensing datasets for lithologic mapping because of its multiple bands, high spatial resolution and relatively low cost. Many methods have been used to detect minerals and rocks from the visible to near-infrared (VNIR) and shortwave infrared (SWIR) bands of ASTER (e.g., Amer et al., 2012; Moghtaderi et al., 2007; Rajendran et al., 2012; Rowan and Mars, 2003; Yamaguchi and Naito, 2003; Zhang et al., 2007b; Zoheir and Emam, 2012), however, silica and silicate minerals do not show prominent spectral features in the

VNIR–SWIR region (Ninomiya et al., 2005; van der Meer et al., 2012; Yajima and Yamaguchi, 2013). These minerals do, however, show specific spectral features in the thermal infrared (TIR) region due to the fundamental vibrations of the Si–O bond (Lyon, 1965). Various studies have shown the great potential of the TIR region for lithologic mapping by airborne remote sensing (e.g., Benkhoff et al., 2006; Kahle and Goetz, 1983; Riaza et al., 2001; Sabine et al., 1994; Vaughan et al., 2003).

The ASTER sensor is the first satellite-borne multispectral TIR remote sensing platform with sufficient spatial (90 m × 90 m), spectral and radiometric resolutions for geological studies (Ninomiya et al., 2005; Yamaguchi et al., 1998; Zhang et al., 2007a). The ASTER TIR data are capable of detecting quartzose, carbonate, mafic–ultramafic and evaporate minerals and rocks. A series of indices have been proposed based on the spectral emissivity features (e.g., Bertoldi et al., 2011; Ninomiya, 2002; Ninomiya et al., 2005; Oztan and Suzen, 2011; Rockwell and Hofstra, 2008; Rowan et al., 2005; Watanabe and Matsuo, 2003; Yajima and Yamaguchi, 2013).

The emissivity products (Level-2B, hereafter L-2B) are derived from the TIR radiance data (Level-1B, hereafter L-1B) using the temperature/

* Corresponding author. Tel.: +86 10 82321796; fax: +86 10 82322095.

E-mail address: liuxncugb@163.com (X. Liu).

emissivity separation algorithms; however, the algorithms are generally complicated and problematic and are still in the validation phase of development (Cheng et al., 2008; Gillespie et al., 1998; Li et al., 2013; Ninomiya, 2002; Peres and DaCamara, 2004). The L-1B product lacks the uncertainties that arise from the atmospheric correction and temperature/emissivity separation algorithms (Ninomiya et al., 2005). Because it is relatively easy to access these data, the indices are widely applied to the L-1B radiance data (Aboelkhair et al., 2010; Matar and Bamoussa, 2013; Ninomiya, 2002; Ninomiya et al., 2005; Rajendran et al., 2011). Nevertheless, the indices are essentially defined depending on the emissivity features of the minerals, despite the interference from the surface temperature and atmosphere. We believe that the indices directly derived from L-1B radiance data should be more effective and accurate than the emissivity based indices when using L-1B radiance data for the detection of specific minerals and rocks.

Another problem is the high degree of correlation between any two ASTER L-1B TIR bands, which implies that the independent information provided by different bands may be limited (Chen et al., 1999). The most widely used decorrelation algorithms are principal component analysis (PCA) and decorrelation stretch (DS), and PCA is the theory basis of DS (Gillespie et al., 1986). PCA algorithm is essentially a dimension reduction method; it is to say that the original information provided by the data will be recombined (Reid and Spencer, 2009), so it may sometimes conceal the spectral features which are useful to detect specific minerals and rocks.

In this paper, we attempt to explain the correlation by a linear approximation to the Planck function and then take advantage of the correlation and regression residual theory to deduce several rock indices for mafic-ultramafic rock and quartz-rich rock from ASTER L-1B TIR data. These methods will be suitable for detecting these rocks in regions of high elevation.

2. Materials

2.1. Study area

The study area (Fig. 1) is located in northern Qinghai Province, China, on the northern edge of the Qinghai-Tibet Plateau. Vegetation overlaps the quaternary strata in July and August because of the plateau continental climate in this area. The average elevation of this area is approximately 4200 m, so there are snow and ice during much of the

year, with minimum snow cover occurring in July and August (Zhao and Chen, 1999).

The study area was chosen based on field work and remote sensing image, and site where the rocks are relatively well exposed, but there is still vegetation in the area, as shown in Fig. 3. Study area A is the primary region interest of study. The lithology of the region A is mainly mafic-ultramafic and quartz-rich rocks (Fig. 2 (a)). The major components of mafic-ultramafic rocks are serpentinite and gabbro. There are minor mafic rocks distribute in lower volcanic groups of Ordovician age. The quartz-rich rocks mainly distribute in the lower Ordovician sandstone-slate group. The major component of quartz-rich rocks in this area is sandstone. There is almost no carbonate rock exposed in this area.

Study area B was chosen for the purpose of extracting carbonate rock formations. The predominant exposed geological formation of this area is Precambrian gneiss group in which the carbonate rocks mainly distribute (Fig. 2(b)). Marble, dolomite and limestone are the major type of carbonate rocks. Moreover, the other rock types of the area are mainly gneiss, sandstone, slate and quartzite. The band ratios (band6 + band8) / band7 of ASTER SWIR data and band13 / band14 of ASTER TIR emissivity data were used to detect carbonate rock. The above remote sensing methods detected some exposed carbonate rocks (Fig. 4(c) and (d)) though the 1:200,000 scale of the geologic map is not detailed enough to depict these carbonate rock outcrops.

2.2. Data collection and processing

The ASTER L-1B data used in this study were acquired on August 12, 2004. The data were radiometrically and geometrically corrected and radiation-calibrated. The weather that day in the study area was clear, with atmospheric temperature ranging from 7 °C to 17 °C (<http://www.cma.gov.cn/2011qxw/2011qsjcx/>). The L-2B temperature and emissivity data were derived from the L-1B TIR radiance data using the atmospheric correction and the emissivity normalization algorithm (NEM). The NEM hypothesizes that the emissivity in a band arrives at a known maximum value ϵ_{\max} (generally 0.99 or 0.96, 0.99 was chosen in this study), and use the gray body radiance whose emissivity is ϵ_{\max} to calculate brightness temperature T_i of each pixel at different bands. The temperature $T_{NEM} = \max(T_i)$ is substituted into the Planck function to calculate an initial emissivity ϵ_i , and then the ratio method and the maximum and minimum difference method (MMD) were used to

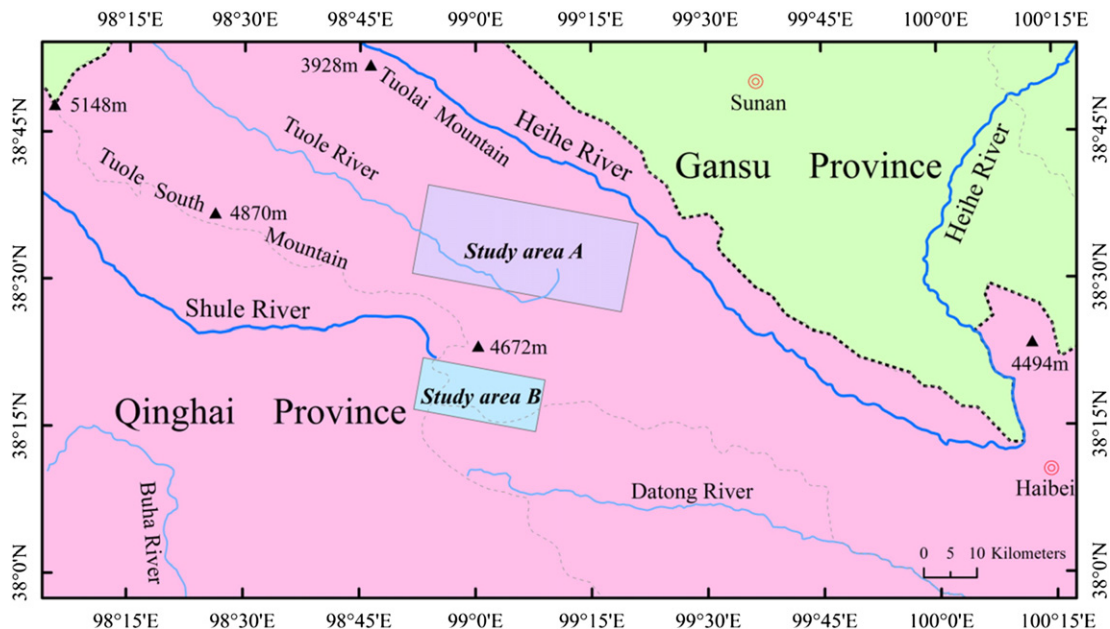


Fig. 1. Geographic map of the study area.

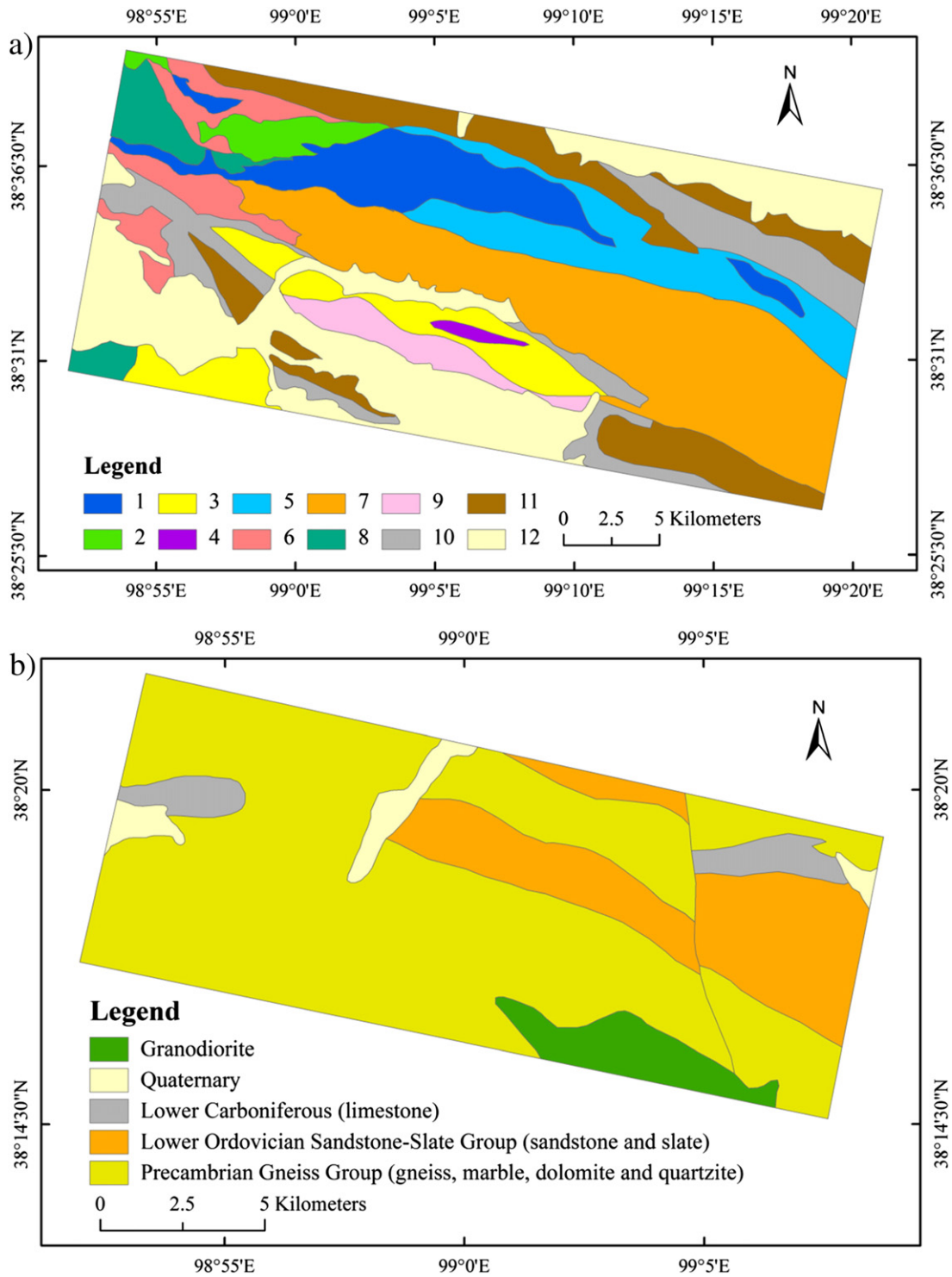


Fig. 2. Generalized lithologic maps of the study areas. (a) Generalized lithologic map of the study area A. Modified from Geology of the Jiahai Region 1:50,000 scale, 1994; Yeniutai Region 1:200,000 scale, 1969; and Wawusi Region 1:200,000 scale, 1986. The numbers in the legend represent geological formations and the predominant rocks of the formation are shown in brackets after the geological formation name: 1, Gabbro; 2, Serpentinite; 3, Felsic rocks; 4, Antimony(Sb)-Lead(Pb) alteration zone; 5, Lower Ordovician Lower Volcanic Group (andesite, breccia and slate); 6, Lower Ordovician Yingou Group (limestone, phyllite and spilite); 7, Lower Ordovician Sandstone-Slate Group (sandstone and slate); 8, Lower Proterozoic (quartzite, schist and gneiss); 9, Precambrian (schist and marble); 10, Upper Carboniferous (sandstone and limestone); 11, Permian (gritstone, quartzose sandstone and balt); and 12, Quaternary. (b) Generalized lithologic map of the study area B. Modified from Geology of the Yeniutai Region 1:200,000 scale, 1969; and Wawusi Region 1:200,000 scale, 1986.

improve the NEM to estimate emissivity and surface temperature more accurately (Gillespie et al., 1998; Tian et al., 2006).

There are a total of five typical categories of surface objects discussed in this paper: mafic-ultramafic rock, quartz-rich rock, felsic rock or mineral, carbonate rock, and vegetation. These rocks and minerals are all

widely distributed in the earth's crust; we do not address minerals and rocks, such as sulfate and phosphate minerals, that are less common in the earth's crust (Tang, 2007). The choice basis of reference samples to the study is listed in Table 1. We selected some points of mafic-ultramafic rock and quartz-rich rock in study area A as samples from the

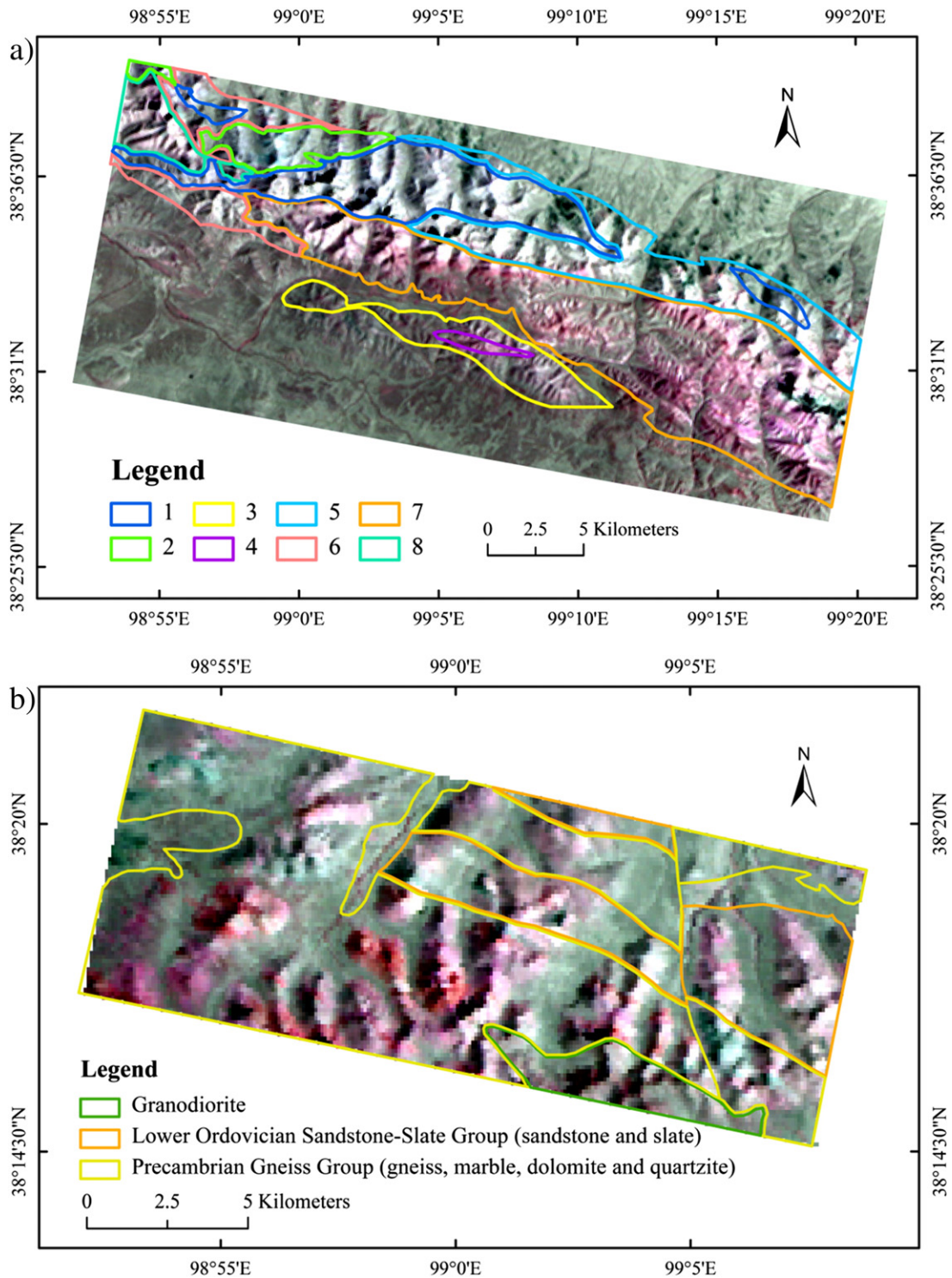


Fig. 3. ASTER L-1B false color composite images (R:G:B = b14:b12:b10) with the boundary of outcrops. (a) Remote sensing image of study area A. The legend numbers are corresponding to that in Fig. 2 (a), and can be referred as in Fig. 2 (a). (b) Remote sensing image of study area B.

ASTER L-1B TIR data based on both the geologic map and remote sensing indices images. We also chose points of vegetation based on an NDVI image of study area A. Sample points of carbonate rock were extracted using the $(b6 + b8) / b7$ and $b13 / b14$ images of study area B. The remote sensing images used to choose samples are shown in Fig. 4. All the indices images were classified into two categories by a threshold value $t_i = \mu + \sigma$, where μ and σ are the

mean and standard deviation value of the indices, separately (Zhang et al., 2003), and the minimum threshold of NDVI was set as 0.15 (Raynolds et al., 2006), as shown in Table 1. The white regions in Fig. 4 represent the detected results for corresponding surface objects. The points were chosen based on the white regions and/or geologic map. About 400 points of felsic rock were chosen based on geologic map (1:50,000 scale), and made sure that these

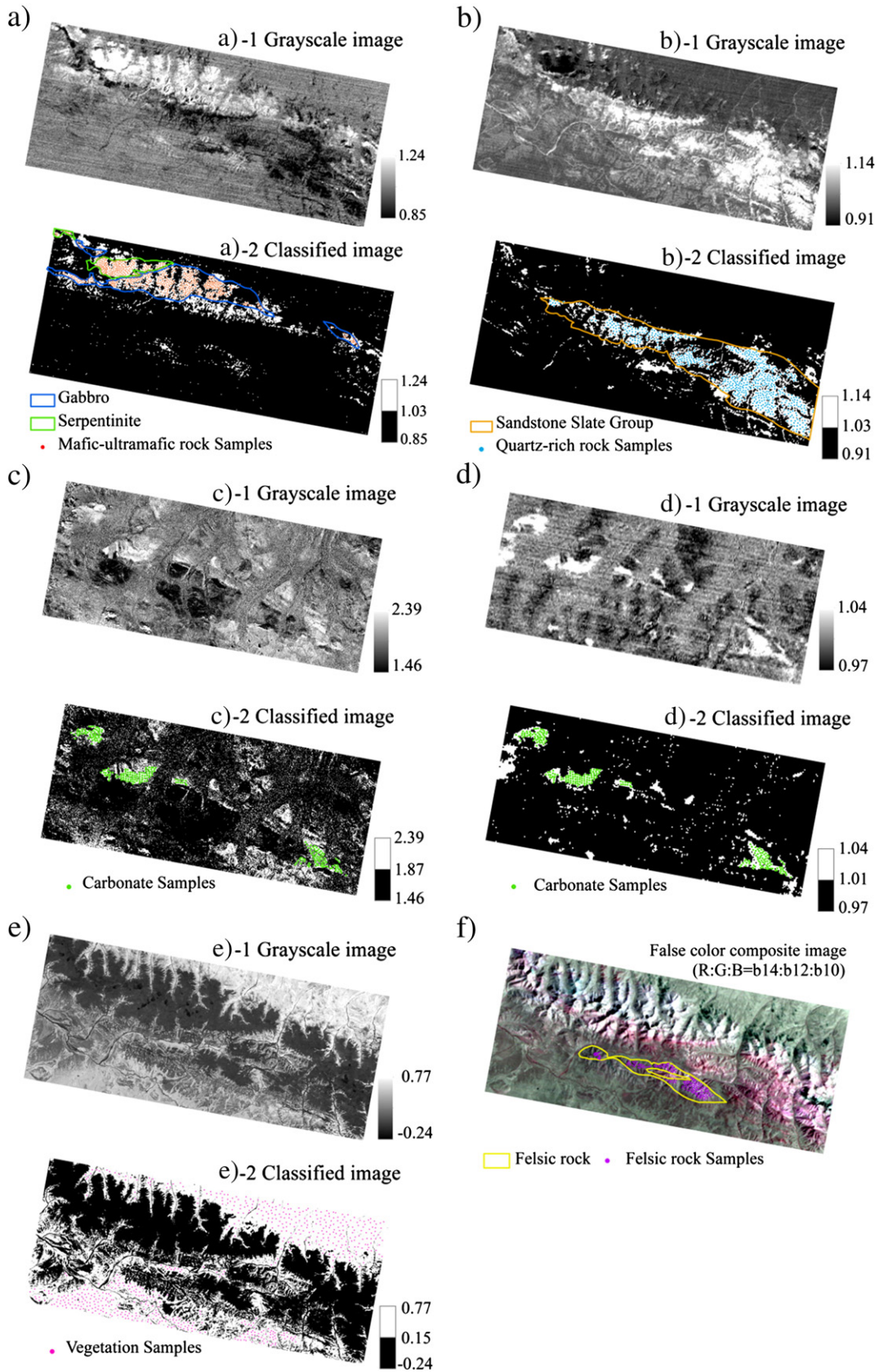


Fig. 4. The remote sensing indices images developed and used to choose points. (a) The $b_{12} * b_{14}^3 / b_{13}^4$ images with the lithologic map for choosing mafic-ultramafic rock samples. (b) The b_{13} / b_{12} images with the lithologic map for choosing quartz-rich rock samples. (c) The $(b_6 + b_8) / b_7$ images for choosing carbonate rock samples. (d) The b_{13} / b_{14} images for choosing carbonate rock samples. (e) The NDVI images for choosing vegetation samples. (f) The chosen samples of felsic rock based on lithologic map.

Table 1
The choice basis of the samples.

	The usage of geological map	The usage of remote sensing indices image/minimum threshold (t)	Level of remote sensing data	Number of points
Mafic-ultramafic rock	Yes	b12 * b14 ³ / b13 ⁴ (Ninomiya et al., 2005) /t = 1.03	L-2B Emissivity data	820
Quartz-rich rock	Yes	b13 / b12 (Rowan et al., 2005) /t = 1.03	L-2B Emissivity data	642
Felsic rock	Yes	–	–	402
Carbonate rock	No	b13 / b14 (Ninomiya et al., 2005), /t = 1.01 (b6 + b8) / b7 (Rowan and Mars, 2003) /t = 1.87	L-2B Emissivity data L-2B Reflectance data	315
Vegetation	No	NDVI /t = 0.15	L-2B Reflectance data	493

points do not distribute in the white regions of the indices images. All these points record the radiance values of all the five ASTER TIR bands and temperature information, and their spatial distributions are approximately uniform.

3. Theory and methods

We attempt to deduce the correlation equations of two ASTER TIR L-1B bands using a linear approximation to the Planck function. We next propose theoretical lithologic indices by integrating the correlation equations with regression residual analysis. The theoretical basis and steps of the derivation are shown below.

3.1. Linear approximation to the Planck function

The total amount of radiance emitted by a blackbody at wavelength λ and temperature T can be described by the Planck function as:

$$B(\lambda, T) = \frac{2hc^2}{\lambda^5} \cdot \frac{1}{e^{hc/\lambda kT} - 1} \quad (1)$$

where h is the Planck constant, c is the speed of light, and k is the Boltzmann constant.

The Planck function is at the heart of the radiation transfer Equation. A linear approximation to the Planck function is the premise for retrieving the land surface temperature from the radiation transfer equation (Mao et al., 2006). First- or second-order Taylor expansions of Eq. (1) are generally used for the approximation. The first two terms of Taylor expansion of the Planck function will achieve a high accuracy (Gao and Qin, 2007; Han and Westwater, 2000; Janssen, 1993; Lipton et al., 2009; Qin et al., 2001). The Taylor expansion of the Planck function at temperature $T = T_0 \approx 300$ K can be expressed as

$$B(\lambda, T) = B(\lambda, T_0) + (T - T_0) \frac{\partial B(\lambda, T_0)}{\partial T_0}. \quad (2)$$

We defined

$$\gamma(\lambda) = B(\lambda, T_0) - T_0 \frac{\partial B(\lambda, T_0)}{\partial T_0}, \quad \varphi(\lambda) = \frac{\partial B(\lambda, T_0)}{\partial T_0}, \quad (3)$$

then Eq. (2) can be simplified as

$$B(\lambda, T) = \varphi(\lambda) \cdot T + \gamma(\lambda). \quad (4)$$

However, because most natural surface objects can't be seen as blackbodies, the radiance is better described as

$$L(\lambda, T) = \varepsilon \cdot B(\lambda, T), \quad (5)$$

where ε is the emissivity. For remote sensing thermal infrared data, the radiance at sensor $L_i^{sen}(T)$ in band i is expressed by

$$L_i^{sen} = \varepsilon_i \cdot B_i(T) \cdot \tau_i + (1 - \varepsilon_i) \cdot L_{ai}^{\downarrow} \cdot \tau_i + L_{ai}^{\uparrow}. \quad (6)$$

where ε_i is the mean of ε and $B_i(T)$ is the mean of $B(\lambda, T)$ in band i , τ_i is the atmospheric transmittance, and L_{ai}^{\downarrow} and L_{ai}^{\uparrow} are the atmospheric upwelling path radiance and atmospheric downwelling irradiance, respectively. In order to facilitate the operation, we defined

$$L_{ai} = (1 - \varepsilon_i) \cdot L_{ai}^{\downarrow} \cdot \tau_i + L_{ai}^{\uparrow}. \quad (7)$$

By substituting Eqs. (6) and (7) into Eq. (4), we deduced

$$T_i = \frac{1}{\varepsilon_i \tau_i \varphi_i} \cdot L_i^{sen} - \frac{\gamma_i}{\varphi_i} - \frac{1}{\varepsilon_i \tau_i \varphi_i} \cdot L_{ai}, \quad (8)$$

where φ_i and γ_i are the mean of $\varphi(\lambda)$ and $\gamma(\lambda)$ in band i , separately. A linear equation that represents the relationship between the brightness temperature T_i and land surface temperature T_s of band i was deduced as:

$$T_s = \frac{T_i - w_i}{B_i + C_i \varepsilon_i \tau_i + D_i \varepsilon_i \tau_i^2}, \quad (9)$$

here B_i , C_i and D_i are coefficients, w_i is offset constant term (Mao et al., 2006). We defined

$$\rho_i = \frac{1}{B_i + C_i \varepsilon_i \tau_i + D_i \varepsilon_i \tau_i^2}, \quad (10)$$

thus

$$T_s = \rho_i \cdot (T_i - w_i). \quad (11)$$

For different bands i and j , the following equation was applied:

$$\begin{aligned} T_s &= \rho_i \left(\frac{1}{\varepsilon_i \tau_i \varphi_i} \cdot L_i^{sen} - \frac{\gamma_i}{\varphi_i} - \frac{1}{\varepsilon_i \tau_i \varphi_i} \cdot L_{ai} - w_i \right) \\ &= \rho_j \left(\frac{1}{\varepsilon_j \tau_j \varphi_j} \cdot L_j^{sen} - \frac{\gamma_j}{\varphi_j} - \frac{1}{\varepsilon_j \tau_j \varphi_j} \cdot L_{aj} - w_j \right). \end{aligned} \quad (12)$$

Through a series of conversions, we finally obtained a linear function:

$$L_i^{sen} = \frac{\varepsilon_i \tau_i \varphi_i \rho_j}{\varepsilon_j \tau_j \varphi_j \rho_i} \cdot L_j^{sen} + L_{ai} - \frac{\varepsilon_i \tau_i \varphi_i \rho_j}{\varepsilon_j \tau_j \varphi_j \rho_i} \cdot L_{aj} + \frac{\varepsilon_i \tau_i \varphi_i}{\rho_i} \left(\frac{\rho_i \gamma_i}{\varphi_i} + \rho_i w_i - \frac{\rho_j \gamma_j}{\varphi_j} - \rho_j w_j \right). \quad (13)$$

This linear function gives the relationship between the radiances of bands i and j of the remote sensing data.

The function is exclusive for specific surface objects and may also be suitable for identifying objects. However, the emissivity is generally difficult to confirm, especially for large categories of rocks, because the emissivity is influenced by multiple factors, such as the composition, structure and physical state (e.g., surface roughness and surface temperature) of the surface objects (Tian et al., 2006). Uncertainty in the atmospheric parameters presents another problem. Inversion of these parameters is complicated, which makes the application of this function to reality problematic.

As an alternative, we seek to compute the slope and intercept in Eq. (13) using statistical regression models fitted to samples acquired from ASTER TIR L-1B data to obtain indices of specific rock types.

3.2. Theory of the regression residual analysis

Assuming that two variables x and y conform to the linear regression model

$$y = \beta_0 x + \beta_1 + \alpha, E\alpha = 0, D\alpha = \sigma^2, \quad (14)$$

the unknown parameters β_0 and β_1 are the regression coefficients. The error α is a random variable. We use the observational data to estimate β_0 and β_1 , producing the respective estimated values $\hat{\beta}_0$ and $\hat{\beta}_1$. Thus, the regression equation can be written as

$$\hat{y} = \hat{\beta}_0 x + \hat{\beta}_1, \quad (15)$$

where \hat{y} is the fitted value of y . The residuals of the i th time observation ($\hat{\alpha}_i$) can be expressed as

$$\hat{\alpha}_i = y_i - \hat{y}_i = y_i - (\hat{\beta}_0 x_i + \hat{\beta}_1). \quad (16)$$

The standardized residuals α_i^* can be expressed as

$$\alpha_i^* = \hat{\alpha}_i / \sigma \approx \hat{\alpha}_i / \hat{\sigma}, \quad (17)$$

where $\hat{\sigma}$ is the root mean square error (RMSE). Using the characteristics of residuals, we can express the following derivation from Eq. (17):

$$-2 < \hat{\alpha}_i / \hat{\sigma} < 2. \quad (18)$$

Plugging Eq. (16) into Eq. (18), we can obtain a relational expression as

$$-2 * \hat{\sigma} < y_i - \hat{\beta}_0 x_i - \hat{\beta}_1 < 2 * \hat{\sigma}. \quad (19)$$

If the statistics of an observation (x_i, y_i) fit Eq. (19), then \hat{y}_i is within the 95% confidence interval of y .

3.3. Derivation of the lithologic indices

Different surface objects generally have different linear relationships between two bands of ASTER L-1B TIR data. If we set the radiance of either of two ASTER TIR bands of a specific rock or mineral as the dependent variable L_i (the radiance of band i), and the radiance of other band as the independent variable L_j (the radiance of band j), and assume that they conform to the linear regression model, then

the relationship between L_i and L_j , based on Eq. (19), can be expressed as follows:

$$-2 * \hat{\sigma} < L_i - \hat{\beta}_0 L_j - \hat{\beta}_1 < 2 * \hat{\sigma}. \quad (20)$$

Surface objects that conform to Eq. (20) are inferred to be the specific rock or mineral that the equation describes. Thus, a rock index can be deduced and expressed as

$$I = L_i - \hat{\beta}_0 L_j - \hat{\beta}_1, \quad (21)$$

and the thresholds t_i of that index can be defined as

$$t_i = \pm 2 * \hat{\sigma}. \quad (22)$$

4. Results and discussion

4.1. Determination of sensitive spectral band

To show the distribution and correlation of the radiances of typical rock types, a scatter plot (Fig. 5) was generated using the radiances of the samples in any two ASTER L-1B TIR bands. The plot exhibits the following information.

- (1) All the surface objects show obvious linear relationships between any two ASTER TIR bands, as we expected based on the explanation in Section 3.1. It is worth noting that the distributions of surface objects are approximately parallel in the plot. The slope a in Eq. (13) is expressed as

$$a = \frac{\varepsilon_i \tau_i \varphi_i \rho_j}{\varepsilon_j \tau_j \varphi_j \rho_i}. \quad (23)$$

The slope of a specific surface object is determined mainly by $\varepsilon_i / \varepsilon_j$. The approximately parallel distributions may be because the differences in emissivity of different objects are relatively small, causing similar values of $\varepsilon_i / \varepsilon_j$ for different objects. For this reason, we suggest that the intercept in Eq. (13) can be used as the primary quantity to discriminate surface objects from one another.

- (2) Fig. 5 (a), (b), (e) and (j) indicate that adjacent L-1B TIR bands generally cannot distinguish well among different categories of surface objects because the objects show similar distribution in these figures. We emphasize that bands 12 and 13 should not be considered as adjacent TIR bands because they have a prominent wavelength gap (b12: 8.925–9.275 μm , b13: 10.25–10.95 μm). It was demonstrated that bands 10, 11, and 12 contain information about both spectral emissivity and surface temperature, with the influence of surface temperature dominating in bands 13 and 14 (Yajimai and Yamaguchi, 2013). Therefore, bands 10, 11 and 12 are in one spectral group, while bands 13 and 14 are in a different group. Although the reliability of the carbonate rock index $CI = b13 / b14$ using L-1B radiance data has been demonstrated, we note that it will be easily disturbed by other surface objects because their distributions in Fig. 5 (j) are very close.
- (3) In Fig. 5 (c) and (f), quartz-rich rock and mafic-ultramafic rock appear distinct, but the distribution of vegetation, carbonate rock and felsic rock overlaps with each other and with quartz-rich rock and mafic-ultramafic rock. The band combinations are suitable for detecting mafic-ultramafic rock because the degree of interference from other surface objects is relatively low.
- (4) Fig. 5 (d) and (g) are similar to each other in that none of the surface objects are distinguished well. Quartz-rich rock and felsic rock have similar distributions. Mafic-ultramafic rock,

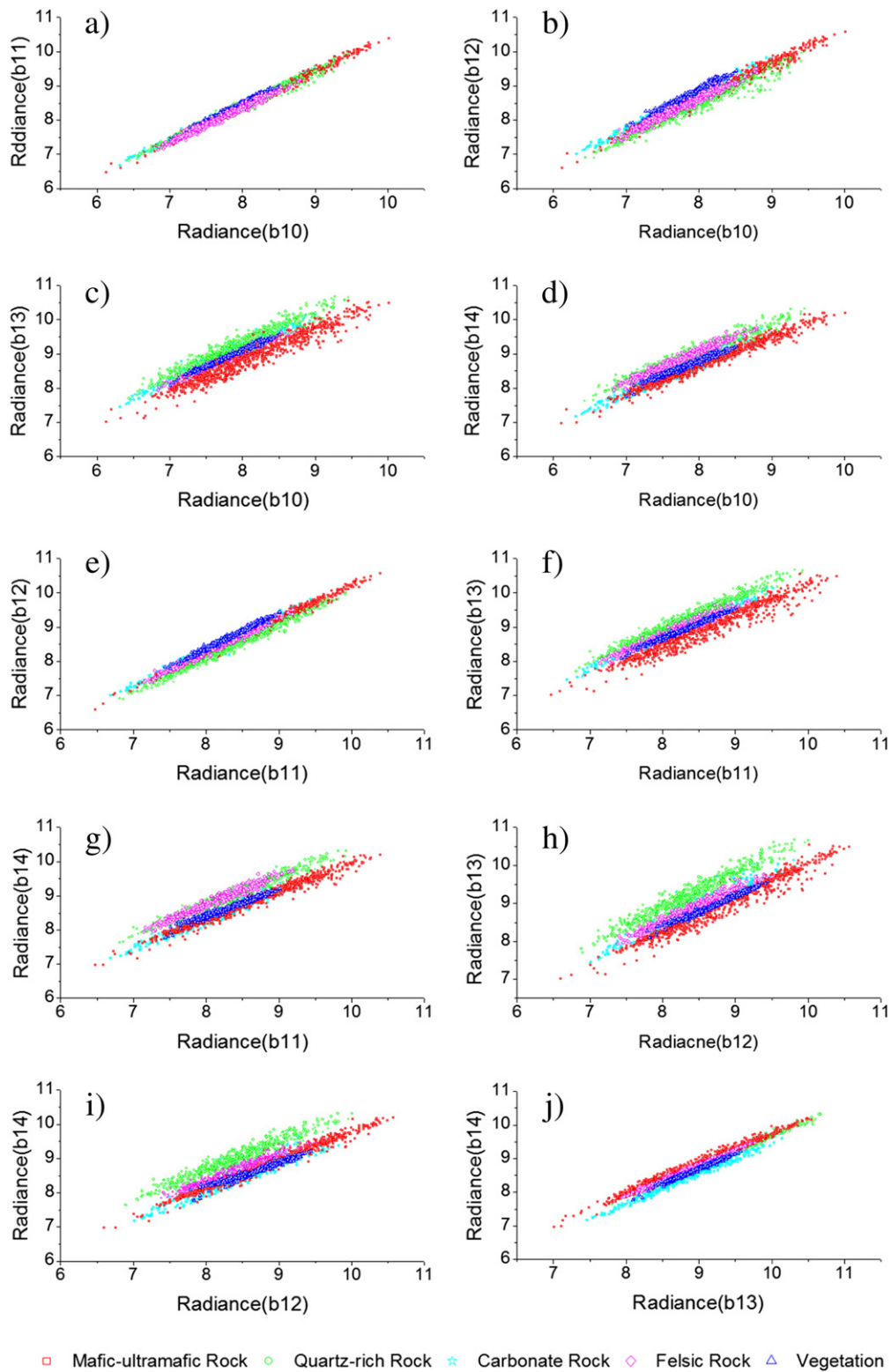


Fig. 5. Scatter plots of radiances of any two ASTER TIR bands. The radiance of the longer-wavelength band is always shown along the y-axis.

carbonate rock and vegetation have similar distributions that are different from those of quartz-rich rock and felsic rock.

- (5) Fig. 5 (h) and (i) indicate that the band combinations b13:b12 or b14:b12 can be used to identify quartz-rich rock. However, the distribution of felsic rock is close to that of quartz-rich rock, therefore felsic rock may interfere somewhat with the detection of quartz-rich rock using these two band combinations.

In summary, the scatter plot indicates that it is possible to map mafic-ultramafic rock and quartz-rich rock using ASTER L-1B TIR data.

As discussed above, linear regression analysis was carried out for four band combinations: b13:b10 and b13:b11 for mafic-ultramafic rock, and b13:b12 and b14:b12 for quartz-rich rock.

The regression results are displayed in Table 2 and Fig. 6. All the regression equations have high R^2 and low RMSE. Consequently, the

Table 2

Regression analysis results of the four band combinations.

Rock type	Band combination	Regression equation	R ²	RMSE
Mafic–ultramafic rock	b13:b10	$\hat{y} = 0.9147x + 1.4366$	0.9437	0.1607
	b13:b11	$\hat{y} = 0.8945x + 1.2404$	0.9425	0.1624
Quartz-rich rock	b13:b12	$\hat{y} = 0.9261x + 1.4623$	0.9415	0.1364
	b14:b12	$\hat{y} = 0.8440x + 1.8971$	0.9316	0.1352

results conform with that the linear correlation between two ASTER L-1B TIR bands is significant.

Fig. 6 shows the regression lines and 95% confidence ellipses of the estimated values of the independent variables. Carbonate rock, felsic rock and vegetation partially distribute at the upper boundary of the ellipses in Fig. 6 (a) and (b). In Fig. 6 (c) and (d), partial felsic rock distributes at the lower boundary of the ellipses. A few points of carbonate rock occur in the ellipses in Fig. 6 (c). All these information demonstrate that the method may be suitable to detect mafic–ultramafic rock and quartz-rich rock using these band combinations, however, there is some interference, primarily from felsic rock and vegetation.

4.2. Development of the lithologic indices

4.2.1. Mafic–ultramafic rock indices

Based on Eq. (21) in Section 3.3, indices for mafic–ultramafic rock (MI) were defined as

$$MI_1 = b13 - 0.9147 * b10 - 1.4366,$$

$$MI_2 = b13 - 0.8945 * b11 - 1.2404.$$

Mafic–ultramafic rocks generally have low index values, and accordingly show dark in the MI₁ and MI₂ grayscale images. The threshold values range from –0.3214 to 0.3214 for MI₁ and from –0.3248 to

0.3248 for MI₂, based on Eq. (22). The results are presented in Fig. 7 (a) and (c). These figures clearly demonstrate the interference of vegetation and felsic rock on MI. Another problem is that the ultramafic rock was not detected well because a component of ultramafic rock cannot be detected and thus displays as a black color. This is essential because the undetectable part of ultramafic rock has a lower SiO₂ content, which results in a lower emissivity in b13. The index value will decrease with decreases in SiO₂ content in ultramafic rock. Therefore, the threshold should be adjusted to reduce the interference of vegetation and felsic rock and contain more ultramafic rock. We ran a series of repeated tests to define the maximum threshold for MI₁ as 0.15 and for MI₂ as 0.14. Index values below these thresholds represent mafic–ultramafic rock. The distribution of carbonate rock is similar to that of felsic rocks in Fig. 6 (a) and (b), so we anticipate that these thresholds will eliminate interference from carbonate rock. Fig. 7 (b) and (d) show the results with the adjusted thresholds. Fig. 7 (e) shows the comparison of these results with those of MI₃ = b12 * b14³ / b13⁴ with a threshold of 0.89, the boundary between mafic and felsic rocks (Ninomiya et al., 2005). The results indicate that the threshold cannot distinguish mafic and felsic rock well in this area, nor could it eliminate the effects of vegetation. We adjusted the threshold to decrease the interference with felsic rock to roughly the same magnitude as in Fig. 7 (b) and (d). The value was finally determined as 0.93, and the result displayed in Fig. 7 (f) indicates that mafic rock is less detected. Accordingly, we conclude that MI₁ and MI₂ are more suitable to distinguish mafic rock from felsic rock.

4.2.2. Quartz-rich rock indices

The quartz-rich rock indices (QI) were defined as

$$QI_1 = b13 - 0.9261 * b12 - 1.4623,$$

$$QI_2 = b14 - 0.8440 * b12 - 1.8971.$$

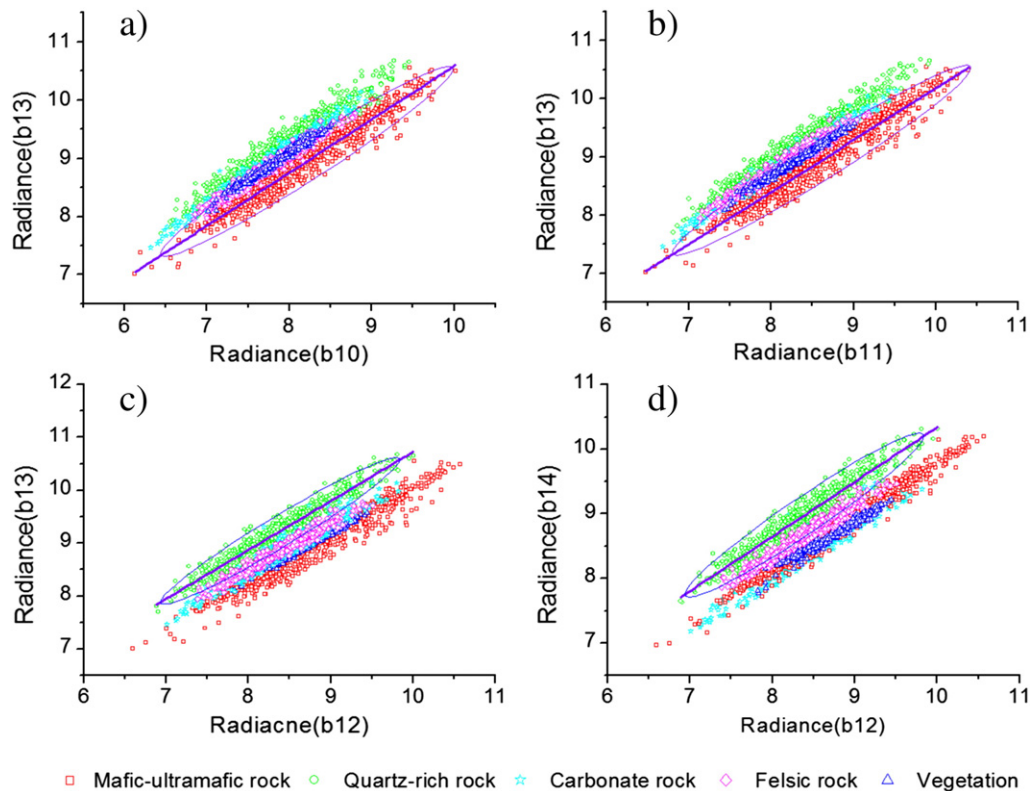


Fig. 6. Scatter plots of the radiances showing regression lines and 95% confidence ellipses. (a) Regression of b13:b10 for mafic–ultramafic rock. (b) Regression of b13:b11 for mafic–ultramafic rock. There is interference on mafic–ultramafic rock in (a) and (b) from other surface objects, such as vegetation, carbonate rock, and felsic rock. (c) Regression of b13:b12 for quartz-rich rock. (d) Regression of b14:b12 for quartz-rich rock. There is interference on quartz-rich rock in (c) and (d) from other surface objects, such as carbonate rock and felsic rock.

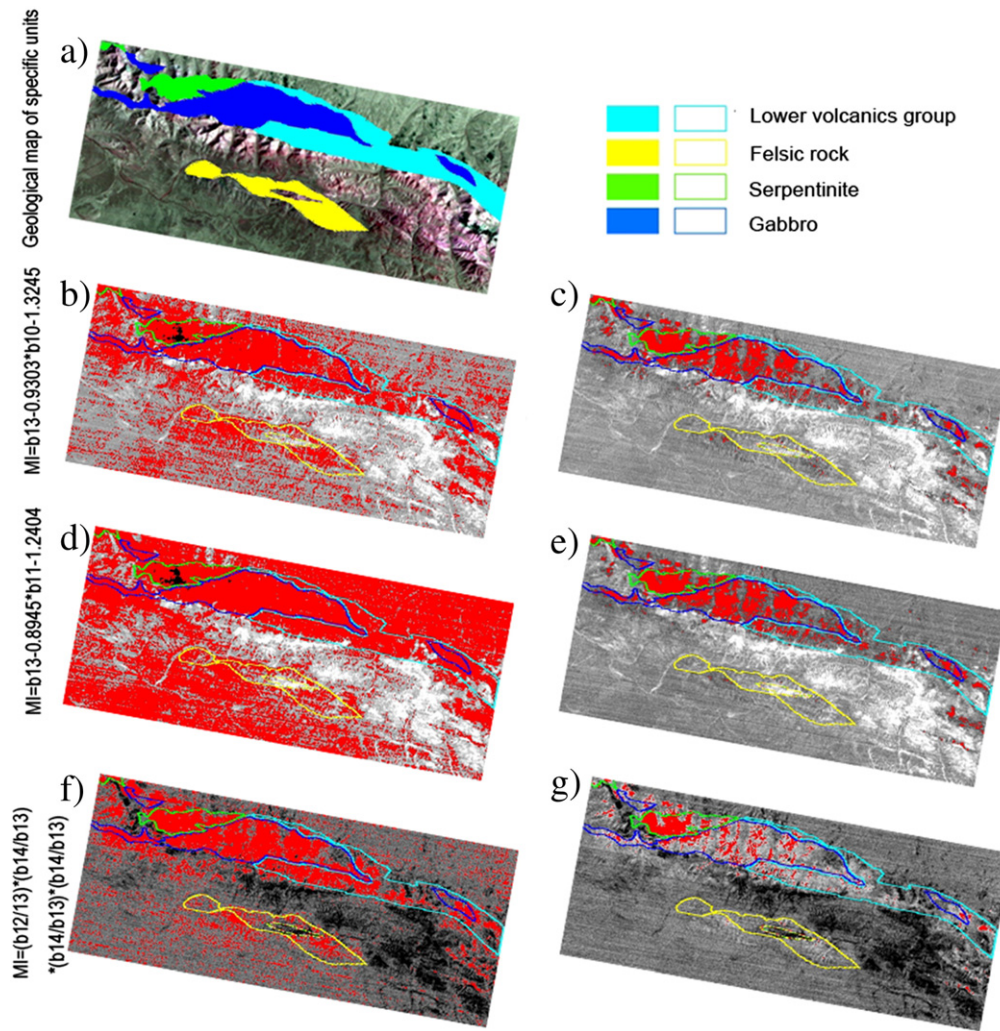


Fig. 7. Detected results of mafic-ultramafic rock by remote sensing indices. (a) Lithologic map of relevant rock units overlaid on an ASTER TIR L-1B false color composite image (R:G:B = b14:b12:b10). (b) Detected region (red) of MI_1 with $-0.3214 < MI_1 < 0.3214$. (c) Detected region of MI_1 with $MI_1 < 0.15$. (d) Detected region of MI_2 with $-0.3248 < MI_2 < 0.3214$. (e) Detected region of MI_2 with $MI_2 < 0.14$. (f) Detected region of MI_3 with $MI_3 > 0.89$. (g) Detected region of MI_3 with $MI_3 > 0.93$.

The segmentation results of the grayscale images of QI_1 and QI_2 using the thresholds calculated by Eq. (22) are shown in Fig. 8 (a) and (b). Few points of felsic rock occur in the detection results and points which were expected to have higher quartz contents are not detected. Therefore, the thresholds calculated from Eq. (22) required adjusting. We set the minimum threshold for MI_1 as -0.2 and for MI_2 as -0.17 . Fig. 8 (f) and (g) show the $QI_3 = (b11 * b11) / (b10 * b12)$ (Ninomiya et al., 2005) and $QI_4 = (b11 * b13) / ((b10 + b12) * b12)$ (Rockwell and Hofstra, 2008) images with minimum thresholds 1.038 and 0.549, respectively. Fig. 8 (f) is too noisy to delineate details; in it, some mafic rocks also display high index value, which were contained in the detected results. However, the alteration zone shows low value in Fig. 8 (f), whereas the values of the alteration zone in other indices are high and promiscuous with quartz-rich rock. It's a weakness of these indices compared to QI_3 . The results in Fig. 8 (g) are similar to that in Fig. 8 (c) and (e). It is difficult to define an effective threshold for QI_4 because the index values are too aggregated: the standard deviation is 0.015 in Fig. 8 (g).

4.3. Stability analysis of the indices

The primary factors that may affect the validity of the indices are surface temperature and atmospheric effects.

The atmosphere in regions of high elevation is relatively thin, so its effect is weak during periods of good weather. Thus, the atmosphere will not significantly interfere with the indices in regions of high elevation. The following is a further and more general discussion. Atmospheric downwelling irradiance (L_{ai}^{\downarrow}) represents 1% to 3% of the total radiance (Xu et al., 1998), so its effect can be ignored. The atmospheric upwelling path radiance can be approximately calculated by

$$L_{ai}^{\uparrow} = (1 - \tau_i(\theta)) \cdot B_i(T_a), \quad (24)$$

where T_a is the average temperature of the upwelling atmosphere (Mao et al., 2006). $\tau_i(\theta)$ is mainly determined by the water vapor content of the atmosphere. Regions where the atmospheric water vapor content is low have high $\tau_i(\theta)$ values and low L_{ai}^{\uparrow} values. This implies that the atmosphere will not significantly interfere with the indices at these regions.

The temperatures and indices values of the sampled points mentioned in Section 2.2 were extracted for mafic-ultramafic rock and quartz-rich rock. The distributions of temperatures of mafic-ultramafic rock and quartz-rich rock are shown in Fig. 9 (a) and (b). They appear to comprise an approximately normal distribution with a mean temperature near 300 K. The statistical characteristics of the temperature data are eligible and acceptable. To clarify the relationship between index

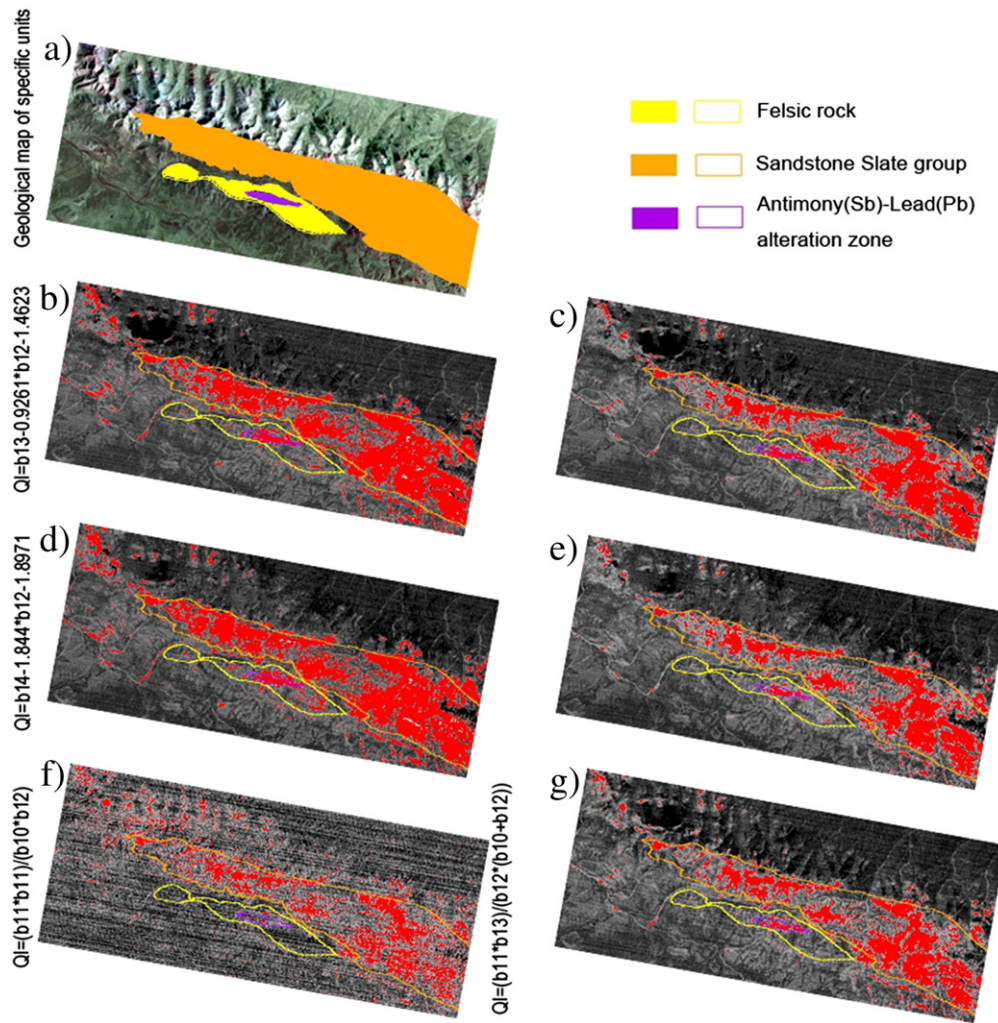


Fig. 8. Detected results of quartz-rich rock by remote sensing indices. (a) Lithologic map of relevant rock units overlaid on an ASTER TIR L-1B false color composite image (R:G:B = b14: b12:b10). (b) Detected region (red) of Q_1 with $-0.2728 < Q_1 < 0.2728$. (c) Detected region of Q_1 with $Q_1 > -0.2$. (d) Detected region of Q_2 with $-0.2704 < Q_2 < 0.2704$. (e) Detected region of Q_2 with $Q_2 > -0.17$. (f) Detected region of Q_3 with $Q_3 > 1.038$. (g) Detected region of Q_4 with $Q_4 > 0.549$.

value and corresponding temperature, the temperature was separated into five levels for mafic-ultramafic rock and four levels for quartz-rich rock as shown in Table 3. The means of the indices at each level are shown in Fig. 9 (c), (d), (e), and (f). The mean values of MI_1 and MI_2 show slight fluctuations near zero, which can be considered stable across the different temperature levels; however, the mean values of Q_1 and Q_2 increase from -0.0496 to 0.0807 in Fig. 9 (d) and -0.0499 to 0.0735 in Fig. 9 (f), as temperatures rise.

To clarify whether the influence of temperature on rock indices is significant, one-way variance analysis (ANOVA) was performed. The indicators are displayed in Table 4. The significance criterion of ANOVA at confidence levels $\alpha = 0.05$ or $\alpha = 0.01$ is given as

$$F \geq F_{\alpha}(s-1, n-s), \quad (25)$$

where s is the number of the temperature level and n is the number of measurements. The F_{α} values shown in Table 4 were obtained from an F-value distribution table (Wu et al., 1995). Based on Eq. (25), we confirm the significance of the difference between each level as represented in Table 4. We found that MI_1 and MI_2 are insensitive to temperature, while Q_1 and Q_2 will be affected by temperature variation, however, $Q_3 = (b11 * b11) / (b10 * b12)$ is insensitive to temperature (Ninomiya, 2002).

This phenomenon may be related to the variation of emissivity with temperature changes. The variation of the emissivity of quartz-rich rock in b13 or b14 is more obvious than it is in b10, b11 and b12, while the variation of the emissivity of mafic-ultramafic rock does not differ greatly among b10, b11 and b13.

Accordingly, we consider that MI_1 and MI_2 are suited to detect mafic-ultramafic rock at regions of high elevation or low atmospheric water vapor content. The thresholds of MI_1 and MI_2 may be robust. However, the thresholds of Q_1 and Q_2 may not always be accurate due to its instability to temperature; therefore, we regard these thresholds as reference values only.

5. Conclusions

This study focuses on deducing rock indices from ASTER L-1B TIR data using a linear approximation to the Planck function. A function was deduced to explain the linear correlation between two TIR bands. Two mafic-ultramafic rock indices and two quartz-rich rock indices were then proposed based on the correlation and regression analysis. A comparison between these indices with other indices defined using the spectral curves of emissivity shows the higher utility of the indices proposed in this study. The primary advantage of these indices is their applicability to ASTER L-1B TIR radiance data. MI shows the potential for detecting mafic-ultramafic rock with reliable thresholds in arid

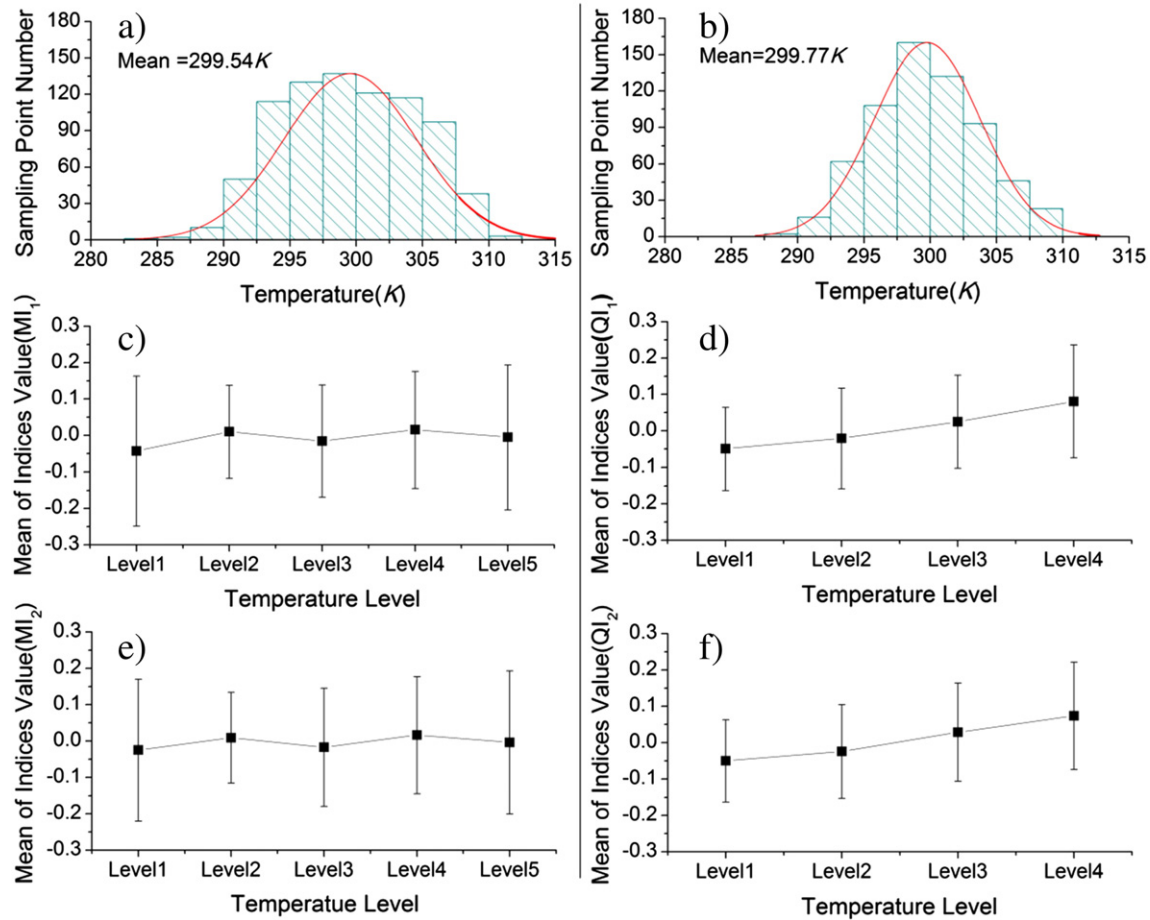


Fig. 9. The distribution of temperature of different rock types and the distribution of indices value at each temperature level. (a) Histogram of surface temperature for mafic-ultramafic rock. (b) Histogram of surface temperature for quartz-rich rock. These plots show the characteristics of the temperature distribution for specific rock types. The mean of the temperature is indicated in the plot. (c), (d), (e), and (f) show the variation of the mean of the index values of MI_1 , QI_1 , MI_2 and QI_2 , respectively, at different temperature levels. Error bars show the standard deviation of the indices value at each temperature level.

regions or regions of high elevation. However, QI may be only suitable for regions such as the Qinghai–Tibet Plateau due to its sensitivity to temperature. These remote sensing indices have the potential to play a significant role in lithologic mapping of regions where geological surveys are difficult.

Notably, the indices proposed in this study derive from semi-empirical models. The parameters are determined by a statistical approach, and the range of application of the indices may be limited. This study is an attempt to apply quantitative analysis to radiance data. More accurate measurements of emissivity and atmospheric

parameters will help to improve the accuracy of the indices. Further modification of the indices based on the mechanism of the spectrum will also improve the capability to detect more categories of minerals and will push the development of geological remote sensing towards a more quantitative direction.

Acknowledgments

This research was supported by the project “Survey and Evaluation of Geology and Mineral Resources of Metallogenic belt at the peripheral and adjacent area of Qaidam Basin, Qinghai province” of China Geological Survey (project ID: 1212011121188). The authors are thankful to the Institute of Geological Survey, China University of Geoscience (Beijing) for providing geological data. Chao Ding would like to acknowledge the help provided by Yaqiong Guan and Feng Ling.

References

- Aboelkhair, H., Ninomiya, Y., Watanabe, Y., Sato, I., 2010. Processing and interpretation of ASTER TIR data for mapping of rare-metal-enriched albite granitoids in the Central Eastern Desert of Egypt. *J. Afr. Earth Sci.* 58, 141–151.
- Amer, R., Kusky, T., El Mezayen, A., 2012. Remote sensing detection of gold related alteration zones in Um Rus area, Central Eastern Desert of Egypt. *Adv. Space Res.* 49, 121–134.
- Benkhoff, J., Helbert, J., Team, M., 2006. Thermal infrared spectroscopy to investigate the composition of mercury – the MERTIS instrument on BepiColombo. *Adv. Space Res.* 38, 647–658.
- Bertoldi, L., Massironi, M., Visona, D., Carosi, R., Montomoli, C., Gubert, F., et al., 2011. Mapping the Buraburi granite in the Himalaya of Western Nepal: Remote sensing analysis in a collisional belt with vegetation cover and extreme variation of topography. *Remote Sens. Environ.* 115, 1129–1144.

Table 3
The range of temperature level of each rock type.

	Level 1	Level 2	Level 3	Level 4	Level 5
Mafic-ultramafic rock	280–290 K	290–295 K	295–300 K	300–305 K	305–315 K
Quartz-rich rock	285–295 K	295–300 K	300–305 K	305–315 K	–

Table 4
Evaluation indicators of ANOVA.

	F value	$F_{0.05}$	$F_{0.01}$	P value	Significance
MI_1	1.65	2.23	3.05	0.16	No
MI_2	1.56	2.23	3.05	0.18	No
QI_1	14.16	2.39	3.36	6.10e-9	Yes
QI_2	15.36	2.39	3.36	1.18e-9	Yes

- Chen, L.F., Zhuang, J.L., Xu, X.R., 1999. The correlation between thermal infrared remote sensing bands and its influence on the inversion of land surface temperature. *Chin. Sci. Bull.* 44, 2122–2127.
- Cheng, J., Liu, Q.H., Li, X.W., Xiao, Q., Liu, Q., Du, Y.M., 2008. The correlation based temperature emissivity separation algorithm. *Sci. China Ser. D Earth Sci.* 38, 261–272.
- Gao, L., Qin, Z.H., 2007. Research on the fitting relation of the Planck equation expansion parameter model in split window algorithm. *Geogr. Geoinf. Sci.* 23, 9–12.
- Gillespie, A., Kahle, A.B., Walker, R.E., 1986. Color enhancement of highly correlated images. I. Decorrelation and HSI contrast stretches. *Remote Sens. Environ.* 20, 209–235.
- Gillespie, A., Rokugawa, S., Matsunaga, T., Cothorn, J.S., Hook, S., Kahle, A.B., 1998. A temperature and emissivity separation algorithm for Advanced Spaceborne Thermal Emission and Reflection Radiometer (ASTER) images. *IEEE Trans. Geosci. Remote Sens.* 36, 1113–1126.
- Han, Y., Westwater, E.R., 2000. Analysis and improvement of tipping calibration for ground-based microwave radiometers. *IEEE Trans. Geosci. Remote Sens.* 38, 1260–1276.
- Janssen, M.A., 1993. *Atmospheric Remote Sensing by Microwave Radiometry*. Wiley, New York 1–35.
- Kahle, A.B., Goetz, A.F.H., 1983. Mineralogic information from a new airborne thermal infrared multispectral scanner. *Science* 222, 24–27.
- Li, Z.L., Tang, B.H., Wu, H., Ren, H., Yan, G., Wan, Z., Trigo, I.F., Sobrino, J.A., 2013. Satellite-derived land surface temperature: current status and perspectives. *Remote Sens. Environ.* 131, 14–37.
- Lipton, A.E., Moncet, J.L., Uymin, G., 2009. Approximations of the Planck function for models and measurements into the submillimeter range. *IEEE Geosci. Remote Sens. Lett.* 6, 433–437.
- Lyon, R.J.P., 1965. Analysis of rocks by spectral infrared emission (8 to 25 microns). *Econ. Geol.* 60, 715–736.
- Mao, K.B., Shi, J.C., Qin, Z.H., Gong, P., Xu, B., Jiang, M.L., 2006. A four-channel algorithm for retrieving land surface temperature and emissivity from ASTER data. *J. Remote Sens.* 10, 593–599.
- Matar, S.S., Bamoussa, A.O., 2013. Integration of the ASTER thermal infra-red bands imageries with geological map of Jabal Al Hasir area, Asir Terrane, the Arabian Shield. *J. Taibah Univ. Sci.* 7 (1), 1–7.
- Moghtaderi, A., Moore, F., Mohammadzadeh, A., 2007. The application of advanced spaceborne thermal emission and reflection (ASTER) radiometer data in the detection of alteration in the Chadormalu paleocrater, Bafq region, Central Iran. *J. Asian Earth Sci.* 30, 238–252.
- Ninomiya, Y., 2002. Mapping quartz, carbonate minerals and mafic-ultramafic rocks using remotely sensed multispectral thermal infrared ASTER data. *Proc. SPIE* 4710, 191–202.
- Ninomiya, Y., Fu, B.H., Cudahy, T.J., 2005. Detecting lithology with Advanced Spaceborne Thermal Emission and Reflection Radiometer (ASTER) multispectral thermal infrared “radiance-at-sensor” data. *Remote Sens. Environ.* 99, 127–139.
- Oztan, N.S., Suzen, M.L., 2011. Mapping evaporate minerals by ASTER. *Int. J. Remote Sens.* 32, 1651–1673.
- Peres, L.F., DaCamara, C.C., 2004. Land surface temperature and emissivity estimation based on the two-temperature method: sensitivity analysis using simulated MSG/SEVIRI data. *Remote Sens. Environ.* 91, 377–389.
- Qin, Z.H., Dall’Omo, G., Karnieli, A., Berliner, P., 2001. Derivation of split window algorithm and its sensitivity analysis for retrieving land surface temperature from NOAA-advanced very high resolution radiometer data. *J. Geophys. Res.* 106, 22655–22670.
- Rajendran, S., al-Khribash, S., Pracejus, B., Nasir, S., Al-Abri, A.H., Kusky, T.M., Ghulam, A., 2012. ASTER detection of chromite bearing mineralized zones in Semail Ophiolite Massifs of the northern Oman Mountains: exploration strategy. *Ore Geol. Rev.* 44, 121–135.
- Rajendran, S., Hersi, O.S., Al-Harthy, A., Al-Wardi, M., El-Ghali, M.A., Al-Abri, A.H., 2011. Capability of advanced spaceborne thermal emission and reflection radiometer (ASTER) on discrimination of carbonates and associated rocks and mineral identification of eastern mountain region (Saih Hatat window) of Sultanate of Oman. *Carbonate Evaporite* 26, 351–364.
- Raynolds, M.K., Walker, D.A., Maier, H.A., 2006. NDVI patterns and phytomass distribution in the circumpolar Arctic. *Remote Sens. Environ.* 102, 271–281.
- Reid, M.K., Spencer, K.L., 2009. Use of principal components analysis (PCA) on estuarine sediment datasets: the effect of data pre-treatment. *Environ. Pollut.* 157, 2275–2281.
- Riaza, A., Strobl, P., Beisl, U., Hausold, A., Müller, A., 2001. Spectral mapping of rock weathering degrees on granite using hyperspectral DAIS 7915 spectrometer data. *Int. J. Appl. Earth Obs. Geoinf.* 3, 345–354.
- Rockwell, B.W., Hofstra, A.H., 2008. Identification of quartz and carbonate minerals across northern Nevada using ASTER thermal infrared emissivity data – implications for geologic mapping and mineral resource investigations in well-studied and frontier areas. *Geosphere* 4, 218–246.
- Rowan, L.C., Mars, J.C., 2003. Lithologic mapping in the Mountain Pass, California area using Advanced Spaceborne Thermal Emission and Reflection Radiometer (ASTER) data. *Remote Sens. Environ.* 84, 350–366.
- Rowan, L.C., Mars, J.C., Simpson, C.J., 2005. Lithologic mapping of the Mordor, NT, Australia ultramafic complex by using the Advanced Spaceborne Thermal Emission and Reflection Radiometer (ASTER). *Remote Sens. Environ.* 99, 105–126.
- Sabine, C., Realmuto, V.J., Taranik, J.V., 1994. Quantitative estimation of granitoid composition from thermal infrared multispectral scanner (TIMS) data, desolation wilderness, northern Sierra Nevada, California. *J. Geophys. Res.* 99 (B3), 4261–4271.
- Tang, H.M., 2007. *Mineralogy and Petrology*. Petroleum Industry Press, Beijing 1–5.
- Tian, G.L., Liu, Q.H., Yu, T., Zhang, Y., Chen, L.F., Li, X.W., et al., 2006. Thermal Infrared Remote Sensing. *Electronics Industry Press*, Beijing 1–232.
- van der Meer, F.D., van der Werff, H.M.A., van Ruitenbeek, F.J.A., Hecker, C.A., Bakker, W.H., Noomen, M.F., et al., 2012. Multi- and hyperspectral geologic remote sensing: a review. *Int. J. Appl. Earth Obs. Geoinf.* 14, 112–128.
- Vaughan, R.G., Calvin, W.M., Taranik, J.V., 2003. SEBASS hyperspectral thermal infrared data: surface emissivity measurement and mineral mapping. *Remote Sens. Environ.* 85, 48–63.
- Watanabe, H., Matsuo, K., 2003. Rock type classification by multiband TIR of ASTER. *Geosci. J.* 7 (4), 347–358.
- Wu, X., Li, Y.L., Hu, Q.J., 1995. *Applied Mathematical Statistics*. National University of Defense Technology Press, Changsha 201–204.
- Xu, X.R., Liu, Q.H., Chen, J.Y., 1998. The remote sensing of land surface temperature. *Acta Sci. Nat. Univ. Pekin.* 34, 248.
- Yajima, T., Yamaguchi, Y., 2013. Geological mapping of the Francistown area in northeastern Botswana by surface temperature and spectral emissivity information derived from Advanced Spaceborne Thermal Emission and Reflection Radiometer (ASTER) thermal infrared data. *Ore Geol. Rev.* 53, 134–144.
- Yamaguchi, Y., Kahle, A.B., Tsu, H., Kawakami, T., Pniel, M., 1998. Overview of Advanced Spaceborne Thermal Emission and Reflection Radiometer (ASTER). *IEEE Trans. Geosci. Remote Sens.* 36, 1062–1071.
- Yamaguchi, Y., Naito, C., 2003. Spectral indices for lithologic discrimination and mapping by using the ASTER SWIR bands. *Int. J. Remote Sens.* 24, 4311–4323.
- Zhang, X.F., Pamer, M., Duke, N., 2007a. Lithologic and mineral information extraction for gold exploration using ASTER data in the south Chocolate Mountains (California). *ISPRS J. Photogramm. Remote Sens.* 62, 271–282.
- Zhang, Y.J., Yang, J.M., Yao, F.J., 2007b. The potential of multi-spectral remote sensing techniques for mineral exploration-taking the Mongolian Oyu Tolgoi Cu-Au deposit as an example. *Earth Sci. Front.* 14, 63–70.
- Zhang, Y.J., Zeng, Z.M., Chen, W., 2003. The methods for extraction of alteration anomalies from the ETM + (TM) data and their application: methods selection and technological flow chart. *Remote Sens. Land Resour.* 56, 44–49.
- Zhao, J., Chen, C.K., 1999. *Geography of China*. Higher Education Press, Beijing 606–615.
- Zoheir, B., Emam, A., 2012. Integrating geologic and satellite imagery data for high-resolution mapping and gold exploration targets in the South Eastern Desert, Egypt. *J. Afr. Earth Sci.* 66–67, 22–34.